Investigation of the input-output relationship of engineered neural networks using high-density microelectrode arrays

Jens Duru [a,1], Benedikt Maurer [a,1], Ciara Giles Doran [a], Robert Jelitto [a], Joël Küchler [a], Stephan J. Ihle [a], Tobias Ruff [a], Robert John [a], Barbara Genocchi [b], János Vörös [a,*]

[a] Laboratory of Biosensors and Bioelectronics, Institute for Biomedical Engineering, University and ETH Zurich, Gloriastrasse 35, Zurich, 8092, Switzerland
[b] Computational Biophysics and Imaging Group, Tampere University, Arvo Ylpön katu 34, Tampere, 33520, Finland

ARTICLE INFO

ABSTRACT

Bottom-up neuroscience utilizes small, engineered biological neural networks to study neuronal activity in systems of reduced complexity. We present a platform that establishes up to six independent networks formed by primary rat neurons on planar complementary metal–oxide–semiconductor (CMOS) microelectrode arrays (MEAs). We introduce an approach that allows repetitive stimulation and recording of network activity at any of the over 700 electrodes underlying a network. We demonstrate that the continuous application of a repetitive super-threshold stimulus yields a reproducible network answer within a 15 ms post-stimulus window. This response can be tracked with high spatiotemporal resolution across the whole extent of the network. Moreover, we show that the location of the stimulation plays a significant role in the networks' early response to the stimulus. By applying a stimulation pattern to all network-underlying electrodes in sequence, the sensitivity of the whole network to the stimulus can be visualized. We demonstrate that microchannels reduce the voltage stimulation threshold and induce the strongest network response. By varying the stimulation amplitude and frequency we reveal discrete network transition points. Finally, we introduce vector fields to follow stimulation-induced spike propagation pathways within the network. Overall we show that our defined neural networks on CMOS MEAs enable us to elicit highly reproducible activity patterns that can be precisely modulated by stimulation amplitude, stimulation frequency and the site of stimulation.

1. Introduction

The inner mechanisms of the brain are an enigma. However, gaining insight into the fundamental properties of neural and synaptic interplay is necessary to deepen our knowledge of brain (dys-)functionality and to accelerate the process of drug and therapy development for nervous system disease treatments. Moreover, understanding the fundamental rules of memory formation may drive the development of novel, bio-inspired methods that benefit the field of artificial neural networks. A major obstacle to the investigation of neural activity in biological systems is posed by the vast complexity of neuronal ensembles *in vivo* (Jonas and Kording, 2017). Hundreds of billions of neurons and glial cells are present in the human brain and the amount of synapses exceeds these numbers by several orders of magnitude (von Bartheld et al.,

2016). The complexity is highly overwhelming in animals, too. The presumably simple nervous system of the largely used model organism *c. elegans* hermaphrodite consists of precisely 302 neurons. Even such a small number of neurons already presents a remarkably entangled system, which is challenging at best to map and understand (Cook et al., 2019), despite today's availability of a plethora of techniques to study neuronal activity across scales. At the smallest scale, the patch-clamp technique enables the study of single ion channels, which are present in the membrane of neurons. The patch-clamp technique can yield signals with a high temporal resolution and a large signal-to-noise ratio (SNR). However, the complexity and difficulty of the technique make it highly impractical to obtain information from a larger set of neurons in parallel. On the other end of the spectrum of techniques, functional magnetic resonance imaging (fMRI) is widely used. In fMRI, the

neuronal activity in whole brains can be studied at the cost of low spatiotemporal resolution by visualizing the modulation of neuronal metabolism. This indirect measurement of the neuronal activity yields a low temporal resolution of a few seconds per frame (Glover, 2011). A compromise between spatial and temporal resolution is provided by microelectrode arrays (MEAs), which allow extracellular voltage recordings of neural populations. MEAs are applied in *in vivo*, *ex vivo*, and *in vitro* experimental setups. The use of MEAs *in vivo* gained a lot of momentum with the Neuropixels system, which is a MEA on a thin shaft, that can be inserted into specific regions of the brain (Jun et al., 2017). This approach allows for long-term electrophysiological recordings in freely-moving animals. When studying the brain *ex vivo*, brain slices of either animal or human origin can be placed on MEA surfaces. Brain slices preserve the intrinsic cell diversity and neural circuitry of brain tissue (Nogueira et al., 2022). A similar level of complexity can be found in brain organoids, which emerged in the field of *in vitro* neuroscience in the last decade. Brain organoids are small model systems that aim to replicate the intrinsic organization of the brain (Sharf et al., 2022). Since organoids are stem cell-derived systems, they can be used to model neurodegenerative diseases *in vitro* (Lancaster et al., 2013). The use of dissociated cells or cell ensembles, such as spheroids, that are cultured on top of MEA surfaces, poses another *in vitro* approach (Yuan et al., 2020), allowing the study of neuronal behavior outside the circuits formed in the brain by nature. Cells can originate from animal brains or can be derived from induced pluripotent stem cells. Human induced pluripotent stem cells (hiPSC) also provide the opportunity of modeling brain disease *in vitro* (Penney et al., 2019; Miller et al., 2013). However, the complexity of such networks remains large, due to the commonly high cell count and the lack of control over how these cells interconnect. Typically, metrics derived from the spontaneous activity, such as the burst frequency, are used as a read-out (Schröter et al., 2022; Mossink et al., 2021). To provide an *in vitro* neuronal culture with reduced complexity, methods for (neuronal) cell patterning need to be applied. By limiting the possible cell adhesion sites, neurons can be confined spatially into clusters of small neural populations. Providing guidance cues for the axons that emerge from these small populations allows the engineering of neural circuits *in vitro* (Shimba et al., 2019; Forró et al., 2018). Such patterning of neurons can be achieved by various means, however, microstructure-based approaches are most reliable in confining cells, especially over longer periods of time (Aebersold et al., 2016). The guidance of axons within microstructures is based on the axonal edge guidance phenomenon (Renault et al., 2016). Using poly-dimethylsiloxane (PDMS) microstructures it was previously shown that engineered neural networks could be established on standard, low-density glass-based MEAs using both primary rat neurons (Ihle et al., 2022; Forró et al., 2018; Mateus et al., 2022) as well as hiPSC-derived neurons (Girardin et al., 2022a, 2022b). More recently, we have transferred this 'bottom-up' neuroscience technique to complementary metal-oxide-semiconductor (CMOS)-based MEAs, which offer electrode densities orders of magnitude larger than in conventional passive MEAs and reveal the propagation of spontaneous activity in such small, confined neural networks with high spatiotemporal resolution (Duru et al., 2022). In this study, we show methods to establish engineered networks of primary rat cortical neurons using PDMS microstructures paired with novel, planar high-density CMOS MEAs. While previous work was focused on the analysis of spontaneous activity only, this work demonstrates methods to stimulate engineered neural networks electrically with high spatiotemporal resolution and analyze the post-stimulus response across the whole extent of the network. This approach allows the study of the input-output relationship of such networks by varying the site, voltage, and frequency of applied electrical stimuli. We find evidence that networks respond to an electrical super-threshold stimulus with a reproducible early response. This network answer can be visualized utilizing various techniques and provides insights into how the engineered neural networks respond to different input signals. We illustrate the influence of the stimulation site

on the network answer using 'sensitivity maps' which show that the networks are most sensitive to a stimulus applied within microchannels. Finally, we show that we can selectively trigger different activity pathways by varying the stimulation site. The extensive Python-based framework we provide enables easy data acquisition and analysis of the spontaneous and stimulation-induced activity of neural networks *in vitro*. Our platform allows the use of the post-stimulus early response as a functional readout from small, engineered neural networks with unprecedented detail. In contrast to previous work (Ihle et al., 2022), we can track the propagation of induced network activity within individual axons and can allocate the electrical response spatially to the engineered neural network.

2. Materials and methods

2.1. Engineering biological neural networks

2.1.1. CMOS HD-MEAs

CMOS HD-MEAs (MaxOne+, MaxWell Biosystems, Switzerland) with bare platinum or platinum black coated electrodes were used, similar to the device described in detail in a previous publication (Müller et al., 2015). In contrast to the chips used in our previous publication (Duru et al., 2022), these MEAs embody a novel chip, offering a flat surface topology with only minimally protruding electrodes. One chip provides 26,400 recording electrodes, arranged in a grid of 220×120 electrodes at a pitch of 17.5 μm, covering an area of 3.85×2.1 mm^2. Up to 1024 electrodes can simultaneously be used for recording by routing them to available on-chip amplifiers through a switch matrix (Frey et al., 2010). Chips with an electrode size of 7.5×7.5 μm^2 were used for the scanning electron microscope (SEM) imaging, while spike data was obtained from chips with electrodes of 10×10 μm^2 in size. Voltage-controlled stimulation can be performed with 32 independent stimulation buffers, that can be connected to three digital-to-analog (DAC) converters. The DACs can be programmed to deliver three independent stimulation waveforms in parallel (Müller et al., 2015).

2.1.2. PDMS microstructures

For a constrained network topology, 150–200 μm thick poly-dimethylsiloxane (PDMS) microstructures were placed on top of the microelectrode arrays as shown in Fig. 1A. For this work, previously characterized circular structures were used. The design of the microstructure was shown to promote clockwise axonal growth and was described in detail in previous works (Forró et al., 2018; Ihle et al., 2022; Duru et al., 2022). Microstructures were manufactured by Wunderli-chips (Zurich, Switzerland) through a soft lithography process. The two-layer structure allows for the separation of the somata from the dendrites and axons. Somata are confined within the seeding wells (nodes), which are open to the top and have a diameter of 170 μm. Axons and dendrites can enter and grow within the shallow inter-node channels with a cross-sectional area of 10×4 μm^2. Side channels with a 5×4 μm^2 cross-sectional area further promote directionality. Up to 6 independent circuits fit onto the sensing area of the MEA.

2.1.3. Chip preparation

Data from cultures on either new or used chips (on which cells have been cultured before) are presented in this work. New chips were rinsed with ultrapure water (18.2 MΩ/cm Milli-Q, Merck-MilliPore) and subsequently blow-dried with N$_2$. To promote cell adhesion, a poly-D-lysine (PDL, P6407, Sigma-Aldrich) coating was applied to all chips by placing a 50 μL droplet of a 0.1 mg/mL PDL solution in PBS (10010023, ThermoFisher) onto the sensing area. After incubating the PDL for at least 30 min at room temperature, the droplet was aspirated and residuals were washed away by rinsing the chip 3 times with ultrapure water. Subsequently, the chip was blow-dried with N$_2$. On some chips, a secondary laminin coating was applied to test its influence on cell adhesion and viability. For this, laminin (11243217001 or L2020, Sigma-Aldrich)
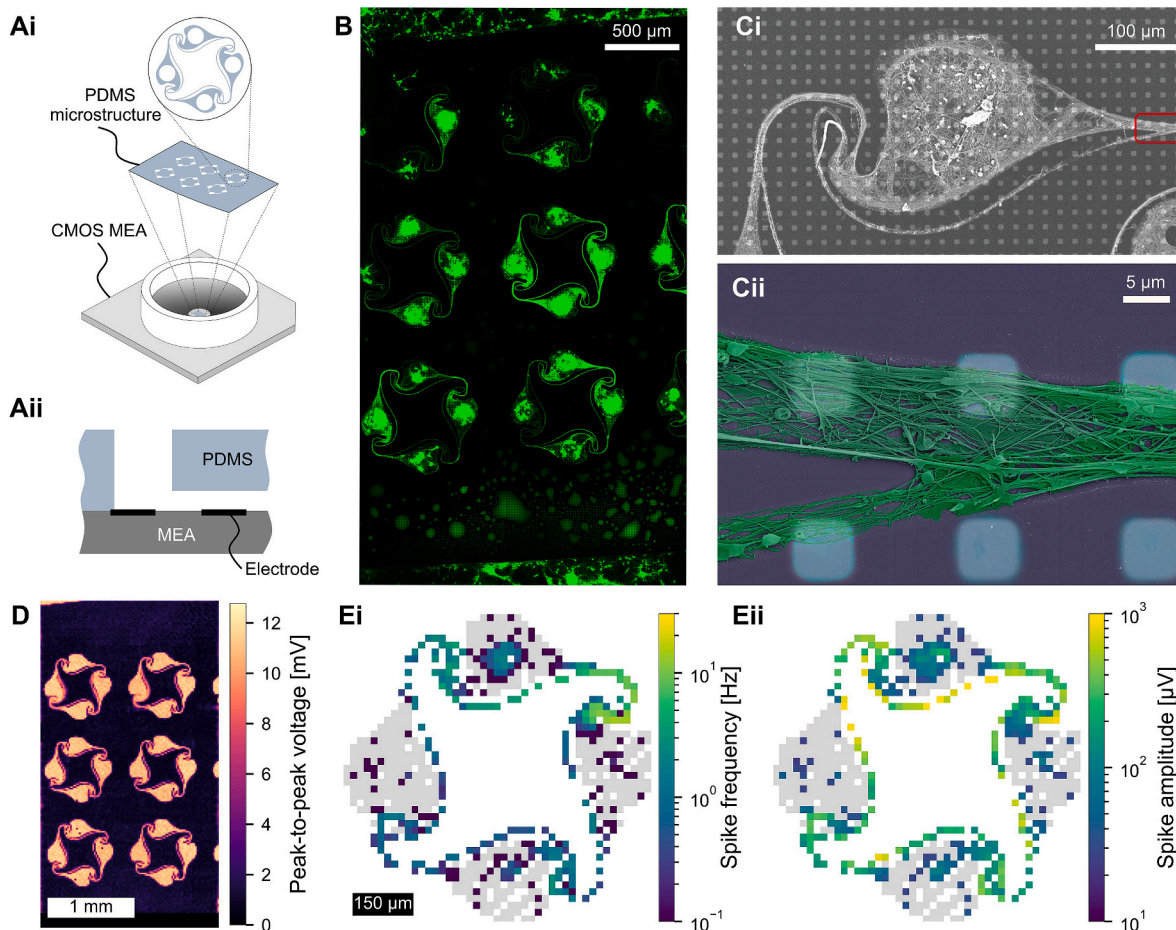
Fig. 1. Primary rat neurons growing inside PDMS microstructures on CMOS MEAs yield topologically constrained neural networks whose activity can be recorded with sub-cellular resolution. (Ai) The PDMS microstructures consist of multiple isolated microfluidic circuits, which are placed onto the sensing area of the CMOS MEA. **(Aii)** Cross section of the PDMS-MEA interface. Due to the planar surface of the chip, the microstructure adheres to the chip with no intermediate layer. **(B)** Engineered neural networks consisting of primary rat cortical neurons growing on the CMOS MEA surface. Multiple neural networks can be established simultaneously on a single chip. The cells were fluorescently labeled using CMFDA and imaged via confocal microscopy at DIV 8. **(Ci)** SEM image showing one node of a network that was fixed at DIV 8 on top of the electrode grid of the MEA. The area marked in red is shown in more detail below. **(Cii)** False-colored SEM image of axons growing inside microchannels on the surface of a CMOS microelectrode array. The axons are precisely confined within the channels. **(D)** Impedance map obtained after microstructure adhesion to the chip. No clogging of channels or delamination of the microstructure is observable. **(Ei)** Spike frequency and **(Eii)** spike amplitude extracted from a 60 s spontaneous recording of an engineered neural network at DIV 15. Signals are amplified in the channels of the microstructure which force axons to the vicinity of the electrodes, while less signal is picked up by the electrodes within the microstructure nodes where somata are present.

with a concentration of 5–20 µg/mL in culture medium or PBS was placed on the sensing area, incubated for 30 min at room temperature and aspirated, before the chip was rinsed 3 times with ultrapure water and dried with N_2. In a next step, the microstructures were cut from the wafer using a scalpel and carefully placed with tweezers onto the sensing area. The microstructures were placed on the chip in such a way that the circumferential reference electrode was not entirely covered and the maximum number of independent circuits was fully accessible by electrodes. The adhesion of the microstructure to the chip surface occurred through electrostatic interactions. Moreover, touching the chip surface was avoided in order to prevent damage to the CMOS MEA. The chip was then filled with 1 mL of PBS. To remove air bubbles trapped inside the microchannels, the chips were placed inside a vacuum desiccator until no more bubbles were visibly emerging from the open seeding wells. To localize the position of the microstructures on the chip, impedance maps were acquired with a custom Python script. The details regarding this method are provided in a previous publication (Duru et al., 2022). To prepare the chip for cell seeding, PBS was aspirated such that the microstructure was still covered in liquid, and replaced with Neurobasal medium (21103049, ThermoFisher) with 1 % B27 supplement (17504001, ThermoFisher), 1 % GlutaMAX (35050-061, ThermoFisher),

and 1 % Pen-Strep (15070-063, ThermoFisher). A cleaning protocol was developed to prepare chips for reuse. For this, the medium was fully aspirated and the microstructure was carefully removed with plastic tweezers, avoiding contact with the chip surface. Then, the chip was placed in a solution of 10 g/L Tergazyme (Alconox, US) for at least 24 h to remove organic material. Afterwards, the chip was placed in 70 % V/V ethanol in deionized water for at least 30 min and subsequently rinsed with deionized water. Until reuse, the chip was stored at 8 °C in deionized water and sealed with parafilm. In total, recordings from 15 different cultures are presented throughout this work. Chips featuring platinum electrodes with (n = 3) and without (7) secondary laminin coating and chips featuring platinum black coated electrodes with (3) and without (2) secondary laminin coating were used.

2.1.4. Cell seeding and maintenance

Primary rat cortical cells of E18 Sprague-Dawley rat embryos (Janvier Labs, France) were used. The use of animal cells was reviewed and approved by the veterinary office of canton Zurich (#ZH048/19). Cells were dissociated following the protocol described in (Duru et al., 2022) and seeded in densities of 30 k or 45 k cells per MEA. The culture medium was exchanged every 3–4 days and on the day before recording

by aspirating roughly 500 µL of the medium and replacing it with 600 µL of fresh medium. The difference of 100 µL accounts for the evaporation of the culture medium inside the incubator.

2.2. Experimental setup

All experiments were conducted inside a custom-built incubator. The CO_2 level was kept constant at 5 % V/V and the temperature was set to 36 or 37 °C. To reduce evaporation, humidity levels were kept above 70 % with one active and one passive water bath. The chips were placed inside a single-well MaxOne Recording Unit (MX1-BRD, MaxWell Biosystems) that was communicating with a connected PC. Custom Python scripts for network selection, data acquisition, processing, and analysis were organized and controlled with a graphical user interface (GUI). The code together with example data is available on GitHub.[2] Supplementary Fig. S14 shows the 'Chip Preparation' tab, for data labeling and network selection. Recording of spontaneous activity and voltage controlled stimulation are grouped in the 'Recording & Stimulation' tab shown in Fig. S15. Some basic data analysis tools used in this work are summarized in the 'Data Analysis' tab as shown in Fig. S16 while more tools for in-depth analysis are available in separate Python classes.

2.3. Data acquisition

2.3.1. Network selection

Networks were selected utilizing the previously mentioned impedance map. A center electrode was manually selected and the electrode grid was restricted to a square of 55 × 55 electrodes. A threshold was subsequently applied, to identify electrodes not covered by the microstructure. Selected electrodes were then routed to available amplifiers and the resulting configuration was downloaded to the chip using the Python application programming interface (API) provided by MaxWell Biosystems.

2.3.2. Voltage recording

The network activity was tracked by recording the voltage on routed electrodes. Voltage recordings were acquired at 20 kHz sampling frequency with a resolution of 10 bit and a recording range of approximately ±3.2 mV, which results in a least significant bit (LSB) corresponding to 6.3 µV. Using custom software based on the MaxWell Python API, the raw traces were recorded and stored as HDF5-files together with the spike times obtained with the system's built-in spike detection algorithm.

2.3.3. Noise analysis

To quantify the influence of the PDMS microstructures on the noise level, signals were recorded before and after the microstructure was placed on the chip. PBS was pipetted onto the chip and the signals were recorded on 1024 evenly distanced electrodes. Afterwards, the PDMS microstructures were attached to the chip and raw signals were recorded on non-covered electrodes within every network for 10 s, again in PBS. The noise level was quantified by determining the average root mean square voltage (V_{RMS}) per routed electrode.

2.3.4. Stimulation protocol

To apply a repetitive stimulation pattern to a network, a custom Python script was created. The script makes use of the MaxWell Python API to send commands to the system hub. While this work only shows data that was acquired by applying a stimulus to a single electrode, our method allows the definition of stimulation patterns on up to 32 independent stimulation electrodes. A biphasic pulse with a leading cathodic phase and 400 µs pulse width was defined with stimulation amplitudes ranging from 100 to 1095 mV. The amplitudes were rounded to the

closest value available on the 10-bit DAC with approximately 3.2 mV step size. This pulse was then defined in a sequence and paired with system delays to yield a stimulation frequency ranging from 1 to 64 Hz. Up to 60 stimulation events were assembled to a stimulation command list and sent for execution to the system hub. 60 events were chosen in order to prevent the hub's queue from overflowing. The command list was then sent to the hub continuously to achieve the desired number of stimulations. Supplementary Fig. S1 illustrates the stimulation procedure.

2.4. Data processing

2.4.1. Raw data processing

Action potential timings were extracted from the voltage traces with a custom spike detection algorithm in Python or the spike detection provided by MaxWell. The custom version first filtered the signals with a second-order Butterworth filter with a corner frequency of 200 Hz. Subsequently, a threshold of 5σ was applied to the traces and a peak detection was performed. Peaks surpassing the 5σ-threshold were considered spikes. To quantify the stimulation artifact, the maximum peak-to-peak voltage occurring within a ±500 µs window around the stimulus onset was determined using the filtered raw signal on every routed electrode.

2.4.2. Stimulus segmentation

Stimulus timestamps were derived by applying a threshold of 315 µV to the absolute amplitude of all spikes detected on the stimulation electrode. All peaks surpassing the threshold were considered as resulting from the stimulation. Blanking was performed by discarding all spikes with less than 10 frames or 0.5 ms distance to the stimulation. The first 15 ms after blanking were treated as the post-stimulus early response. To isolate stimulation-induced effects from spontaneous activity, a threshold was introduced above which electrodes are considered 'active'. This threshold was set to 0.1 spikes on average per electrode per stimulus iteration. For visualization, the post-stimulus response across the whole network can be transformed into a raster plot image following a method adapted from (Ihle et al., 2022). Spikes are represented in a sparse 2D matrix with their latency to the applied stimulus on the horizontal axis and the stimulus iteration on the vertical axis. In some cases, binning is applied to the binary data. Optionally, the matrix can be convolved with a filtering kernel of [0.25, 0.5, 0.25] along the axis of the latency to smooth the spike data. A color code for every recording electrode is derived according to the polar coordinates with respect to a center point of the circular network. The complementary RGB color is multiplied with the spike matrix, scaled by an attenuation factor, and subtracted from a white image.

2.4.3. Propagation analysis

To visualize the flow of information within engineered neural networks on the CMOS MEA, we have developed an algorithm called *NeuroFlow*. The algorithm detects spike events within a user-specified window and correlates them to activity within a spatial and temporal neighborhood. The output of the algorithm is a vector field, whose arrows begin at active electrodes and point into the direction of the subsequent spike detected within the spatiotemporal neighborhood. For the vector fields shown in Fig. 6, two spikes were considered consecutive if they occurred within a temporal window of 200 µs at a maximum distance of 3 electrodes to each other. The end of the blanking period post-stimulus was chosen as the starting point of the analysis.

2.5. Cell culture imaging

2.5.1. Fluorescence imaging

Images of neural cultures on the CMOS MEAs were obtained using a fluorescent dye (CellTracker Green CMFDA, C7025, ThermoFischer). The dye was dissolved in dimethyl sulfoxide (DMSO, 276855, Sigma-

---

[2] https://github.com/lbb-neuron/CMOS_stimulation_and_recording.

Aldrich) and was added to the culture at a working concentration of 1 μM. After an incubation period of 30 min at 37 °C, the culture medium was replaced. The images were acquired using a confocal laser scanning microscope (CLSM, FluoView 3000, Olympus). The details on the imaging procedure can be obtained from a previous publication (Duru et al., 2022). Briefly, a round coverslip with 10 or 12 mm diameter was placed floating within the culture medium on top of the culture. Then the culture medium was aspirated until the coverslip made contact with the epoxy surrounding the sensing area of the chip. Due to surface tension, the coverslip was held into place and the chip could be flipped to be imaged in an inverted microscope.

2.5.2. Scanning electron microscopy of network features

To obtain detailed images and evaluate the adhesion of the cells to the flat CMOS chip surface, scanning electron microscopy (SEM) imaging was performed. Cells were prepared using a standard fixation and dehydration protocol. The samples were fixed with 2 % glutaraldehyde and 2 % formaldehyde for 20 min at room temperature while being placed on a shaker. Afterwards, the PDMS microstructure was removed to expose the cells and the samples were fixed for another 15 min at room temperature, again placed on a shaker. The samples were then washed three times using PBS before dehydrating them in a series of solutions with increasing ethanol concentrations (50 %, 70 %, 90 %, 100 %). Each solution was applied to the samples for 10 min. This process was followed by two further washes in dry ethanol for 60 min each at room temperature. The samples were then critical point dried from ethanol with liquid CO_2 using a critical point dryer (Autosamdri-931, Tousimis, USA). Afterwards, the samples were high vacuum sputter coated with 8 nm Pt–Pd using a CCU-010 (Safematic GmbH, Switzerland) before imaging them using a scanning electron microscope (Merlin, Zeiss). Images were acquired using an InLens SE-detector with an acceleration voltage of 10 kV at a working distance of 18–19 mm.

3. Results and discussion

3.1. Neurons are precisely confined on the CMOS MEA surface

Both confocal as well as SEM imaging revealed that the PDMS microstructures precisely constrain the adhesion of neurons and the growth of axons on the CMOS chip surface. Fig. 1B shows an image of fluorescently labeled networks at DIV 8 (days *in vitro*). Outside of the PDMS microstructure, at the very top and bottom of the sensing area, neurons were able to grow and form random connections. The variation in fluorescence between the networks is mostly due to the different number of neurons confined within the networks. Larger neural populations yield stronger fluorescent signals. In order to visualize the cell adhesion and axonal guidance on the chip in more detail, SEM images were acquired. Fig. 1Ci shows one node and inter-node channel of a network that was fixated at DIV 8. The neurites are confined within the microstructure and no growth is visible in the regions outside the channels and the node. The visible delamination of an axon bundle was most likely induced by the mask removal process since the shape of the bundle resembles the side channel's curvature. The region marked in red is shown in more detail in the false-colored SEM image in Fig. 1Cii. The large amount of axons and dendrites within this channel illustrates how complex these networks remain, despite the efforts in reducing the cell count and complexity overall. We also notice that some small bodies are present within the channels with diameters below 2 μm. Due to their small size, it can be concluded that these bodies are neither neuronal somata, which are roughly 10–20 μm in size (Kriegstein and Dichter, 1983), nor microglia, whose cell bodies measure approximately 5 μm (Kongsui et al., 2014). It may be that what we observe are axonal varicosities, which are enlarged entities found along axons (Gu, 2021). It is hypothesized that these varicosities are locations at which synapses form when unmyelinated axons are involved (Shepherd et al., 2002). In order to perform electrical recordings on the chip, the locations of the

networks need to be determined by the aforementioned impedance scan. Exemplary results obtained using a platinum electrode MEA with no secondary coating are shown in Fig. 1D. Six networks are isolated from each other with no clogging observable in the microchannels. This implies that the simple adhesion step with no intermediate gluing or bonding is sufficient to form a seal between the microstructure and the chip surface. Impedance maps for platinum black coated electrodes and secondary coatings with laminin are shown in the supplementary information in Fig. S2.

3.2. CMOS MEAs allow functional imaging of engineered neural networks with high spatial resolution

Neurons cultured *in vitro* exhibit spontaneous electrical activity upon maturation (Chiappalone et al., 2006). As shown in a previous publication, the spontaneous activity of engineered neural networks on CMOS MEAs yields rich data (Duru et al., 2022): up to 800 electrodes can be routed to pick up the electrical activity from a single network formed using the microstructure design shown in Fig. 1Ai. Hence, the spontaneous electrical activity can be studied with sub-cellular spatial resolution. Fig. 1E shows the spontaneous activity of an engineered neural network recorded at DIV 15 using a CMOS chip with platinum electrodes and a secondary coating of laminin. Similar results can be obtained using chips with platinum black coated microelectrodes and without the usage of laminin as shown in the supplementary information in Fig. S3. It is evident that signals are largest in the channels of the microstructure, reaching spike amplitudes of up to 1 mV at spiking frequencies around 10 Hz. Microchannels are known to amplify extracellular signals (FitzGerald et al., 2008; Lewandowska et al., 2015) because they increase the parasitic leakage resistances (Dworak and Wheeler, 2009). This was reported to increase SNR in microchannels compared to open space recording sites (Pan et al., 2014). In contrast to the microchannels, less activity is recorded within the nodes of the microstructure. The reduced activity observed at these locations may be due to reduced adhesion of the neurons to the electrodes caused by clustering effects, fewer axons in the vicinity of electrodes because of the larger available space, or may be induced through increased noise levels when PDMS microstructures were placed to the chip. We observed an increase in the average noise level per channel from 8.1 μV_{RMS} when no microstructure was present on the chip surface to 16.4 μV_{RMS} (SD: 3.5, *n* = 6 networks, bare platinum electrodes) after microstructure adhesion. We hypothesize that the increase in noise is due to the partial covering of the reference electrode with PDMS. The use of platinum black-coated electrodes has been shown to increase the SNR in comparison with bare platinum electrodes (Viswam et al., 2019). However, in our case, variations in spike amplitude and active electrode count in samples prepared under the same conditions dominated any potential differences induced by the culturing or electrode conditions (see Supplementary Fig. S11). Generally, we were capable of maintaining active cultures for at least 4 weeks *in vitro* before activity dropped (see Supplementary Fig. S12), with individual cultures remaining active for at least 77 DIV.

3.3. Microchannels increase the spatial extent and temporal decay of stimulation-induced artifacts

Applying an electrical stimulus to a stimulation electrode yields a large disturbance to the recording electrodes. This disturbance is known as a stimulation artifact and is due to the fact that the stimulation voltages applied to the stimulation sites are orders of magnitude larger than the physiological signals that the recording amplifiers are optimized for (Ronchi et al., 2019). The artifact can be split into a direct artifact caused by the stimulation pulses delivered through the electronics and a residual artifact, induced by the discharge of residual charge on the electrodes (Zhou et al., 2018). Just like neuronal signals, the stimulation artifacts are enlarged in microchannels (Habibey et al., 2017). CMOS MEAs allow for an analysis of the spatial extent of

stimulation artifacts (Shadmani et al., 2019), however the influence of microchannels on the spatial extent of the stimulation artifact was not characterized before. Fig. 2 shows the dependency of the spatial and temporal behavior of the stimulation artifact depending on the stimulation site. The data was obtained using a neural culture at DIV 14 that showed neither spontaneous nor stimulation-induced activity. A biphasic pulse with a pulse width of 400 μs and stimulation amplitudes of 250, 500, and 750 mV was applied at a frequency of 4 Hz to an electrode within the side channel, the inter-node channel, and within the node. In general, a stimulus applied within a microchannel yields an artifact that spreads along the channel. Up to 54 neighboring amplifiers saturated when a 750 mV stimulus was applied to an electrode in the center of the inter-node channel. A stimulation occurring within a node of the microstructure yields a highly localized artifact. The confinement inside the PDMS microstructure was tested by routing a dense 23×23 electrode patch around the stimulation electrode. Fig. 2B demonstrates that the electric field emerging from the stimulus remains confined within the microchannel with only a reduced artifact observable outside the microstructure boundaries. With no means to suppress the artifact on the CMOS chip, we observe a large difference in the temporal behavior of the post-stimulus signals as shown in Fig. 2C. The stimulation artifacts on neighboring electrodes decayed rapidly in case the stimulus occurred within the node, while the decay on neighboring electrodes was much slower when a stimulus occurred within the microchannels. In the case of inter-node channel stimulation, the directly neighboring electrodes (distanced one and two electrodes from the stimulation site) did not recover within the 250 ms inter-stimulus interval. Blinding of neighboring electrodes due to an artifact could lead to information loss at electrodes very close to the stimulation site. However, as seen in Fig. 2C, electrodes 4 units away from the

stimulation site are available for recording after a few milliseconds. The discrepancy in the behavior between the inter-node and the smaller side channel may be due to partial coverage of the electrode in the latter case. As seen in Fig. 1Cii, microelectrodes are sometimes partially covered, which influences the area available for charge injection during stimulation. Hence, a partially covered electrode may induce smaller electric fields post-stimulus and therefore artifacts. The enlarged spatial extent of the stimulation artifact might be indicative of an enhanced stimulation efficiency in microchannels. The behavior on all neighboring electrodes as well as the full temporal behavior of the inter-node stimulation artifact is shown in the supplementary information in Fig. S4.

3.4. Repetitive super-threshold stimulation yields a reproducible post-stimulus early response

The electrical stimulation of neurons using microelectrode arrays is an established method to induce activity in neurons and neural cultures (Obien et al., 2015). The approach we follow allows the application of a stimulus to any electrode underlying the network and track the immediate early response of the network. Fig. 3A shows the latency of the first spike detected on an electrode after a 4 Hz, 500 mV stimulus was applied to the network for three stimulation iterations at different time points t_0. A video showing the propagation of this activity is provided in the supplementary movie SM1 (Supplementary Fig. S17 shows a single frame at approximately t = 1 ms after stimulation). It is visible that the early response of the network to the stimulus is reproducible, *i.e.* the flow of information through the network is identical for a constant, super-threshold stimulus. In order to visualize the early response for repetitive stimulation in a compressed fashion, a post-stimulus raster plot can be generated. The concept is shown in Fig. 3B and is described
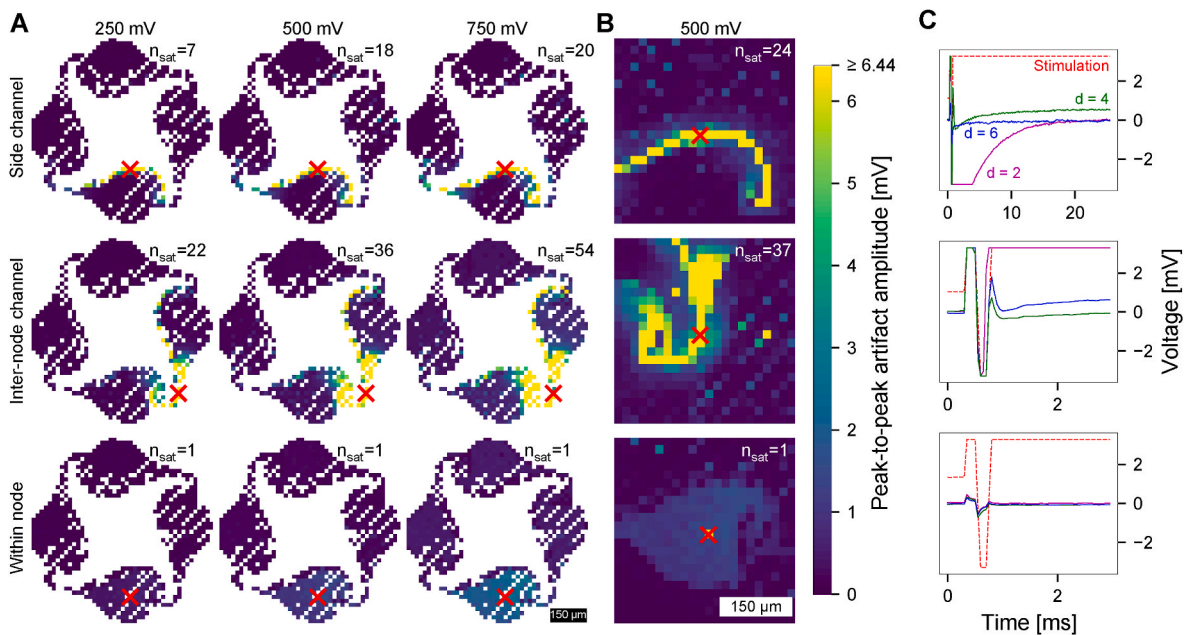

Fig. 2. Quantitative analysis of the stimulation artifact induced by electrical stimulation in microchannels and open space. The upper row describes the behavior when a stimulus is applied to an electrode in a side channel, while the middle and lower rows describe the behavior when a stimulus is applied to an electrode in an inter-node channel and within a node, respectively. **(A)** The magnitude of the stimulus artifact is defined as the maximum peak-to-peak voltage amplitude detected at each electrode after stimulation. The spatial extent of the stimulation artifact is dependent on the stimulation site (marked by a red cross) and the stimulation voltage. A stimulus applied to a microelectrode within the side or inter-node channel of a circuit causes stimulation artifacts that are spreading widely across the channel compared to when the stimulation electrode is located within the node, which can be considered an open space. The number of amplifiers forced into saturation during stimulation (n_{sat}) is given in the top right corners. **(B)** A dense routing around the stimulation site demonstrates that the artifact is recorded only at electrodes that are not covered by PDMS, indicating that the electric field is confined in the microchannels. **(C)** The temporal decay of the stimulation artifact on neighboring electrodes is dependent on the stimulation electrode site. The raw signals of the amplifiers connected to the stimulation electrodes as well as neighboring, non-covered electrodes with a distance of $d = 2$, 4 and 6 electrodes to the stimulation site are shown. The biphasic stimulation pulse is centered around 0.5 ms. Artifact voltage signals recorded on neighboring electrodes show higher amplitudes and a slower decay when a stimulus is applied inside the microchannel. In comparison, a stimulus applied to an electrode within the node yields a large artifact only at the amplifier connected to the stimulation electrode.
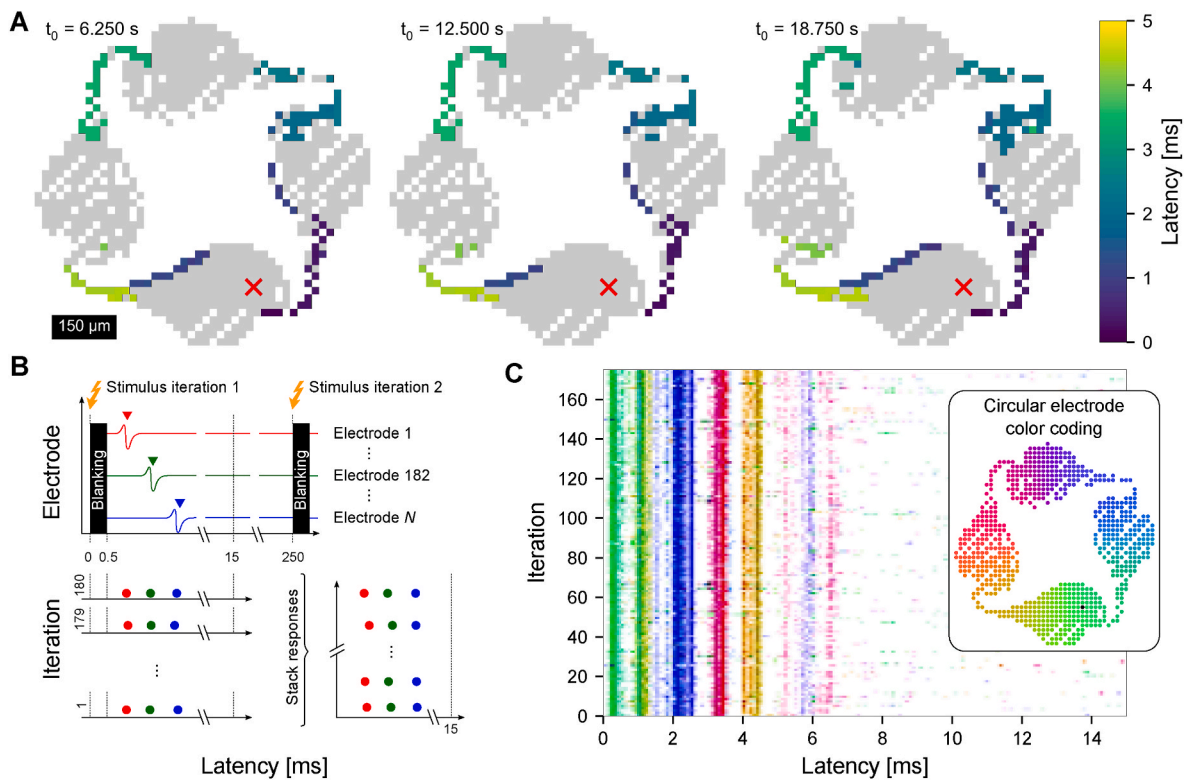
Fig. 3. Analysis of the post-stimulus response reveals a reproducible network response. (A) Stimulating a network at DIV 20 with a 4 Hz biphasic stimulus with an amplitude of 500 mV yields a reproducible immediate network response. Shown here are three network responses during the stimulation experiment with the stimulus onset t_0 given on top. First detected spikes on the recording electrodes are represented based on their latency with respect to the stimulus. **(B)** Procedure for repetitive stimulation, binary spike data extraction and segmentation. A stimulation pattern is repeated (here 180 times), while the signal is recorded at N (up to 1024) electrodes. Spikes after a blanking period of 0.5 ms are detected and used for further analysis. By stacking the responses of individual stimulus iterations in the y-direction, a post-stimulus raster plot is generated. **(C)** Post-stimulus raster plot obtained using the same stimulation parameters as in **A**. Similar latencies over multiple iterations appear as 'bands' in the raster plot. *Insert*: By applying a circular color-coding to all electrodes, the spike time information from the raster plot can be linked to the electrode location. The stimulation site is indicated by a black dot.

in the methods section. Binarizing the spike events and stacking them, while maintaining a color code to assign spikes in the raster plot to the location at which they occurred within the network yields the emergence of 'bands' (Bakkum et al., 2008). Such bands are indicative that the network's early response to a stimulus is reproducible over all iterations and can also be utilized to indicate adaptations or general changes in the network response over time (Ihle et al., 2022; Reinartz et al., 2014). Applying these methods to data obtained from engineered neural networks on CMOS MEAs allows the illustration of the location and temporal dynamics of network activity. Fig. 3C shows the network post-stimulus raster plot for the same data shown in Fig. 3A. Using the circular color code illustrated in the figure insert, the locations of the many occurring bands can be linked to spatial coordinates. The bands appear as straight lines with a short latency and high probability of occurrence over multiple iterations, which indicates that they are likely directly evoked (Bakkum et al., 2008).

3.5. Changes in the post-stimulus early response occur at specific thresholds

By applying a stimulation protocol in which the stimulation voltage is gradually changed, we can observe at which applied voltages the network response changes. Fig. 4A shows the spatial distribution of the network's early response to a stimulus of 370 mV and 450 mV. Every dot stands for an electrode with its size representing the average number of spikes detected per stimulus iteration. The black dot indicates the stimulation site. A large spike count is observed in the microchannels. The larger stimulation voltage yields a more pronounced network response, *i.e.* an increase in early response spiking activity. Averaging

the spike count over all active electrodes yields the plot shown in Fig. 4B. When the stimulation amplitude is low, the average number of spikes per active electrode remains at the level of the expected spontaneous activity around the chosen threshold. An increase in the spike count occurs when the stimulation voltage surpasses roughly 370 mV. These observations align with previously published dynamics (Ihle et al., 2022). From there, the spike count successively increases with an increase in stimulation voltage until saturation is reached at about 450 mV.

The temporal information of the early response is shown as post-stimulus raster plots in Fig. 4C. While no stable response is observable at a stimulation amplitude of 300 mV, bands emerge at larger amplitudes. The raster plots corresponding to a stimulation amplitude larger than 500 mV show remarkably little variations. The gradual change in the early response within the transition period is visualized in Fig. 4D. Here, the post-stimulus raster plots are shown for consecutive stimulations with an increase in the stimulation voltage of 5 mV. We observe the emergence of bands (magenta and orange) at a latency of 7–8 ms. The bands become gradually stronger since the probability of recording spikes in these bands increases and reaches saturation already at 380 mV along with a gradual shift towards a higher latency. Such latency shifts could potentially be caused by plasticity effects that arise through the continuous stimulation of the network. A stimulation voltage of 400 mV yields the emergence of a blue band and another faint magenta band, which possibly represents the recruitment of more axons activated by the stimulus. The jump of the magenta bands towards earlier latencies could be attributed to either a change in the spike detection threshold or a different activation of the underlying network architecture. The occurrence of spikes before 5 ms post-stimulus may increase the
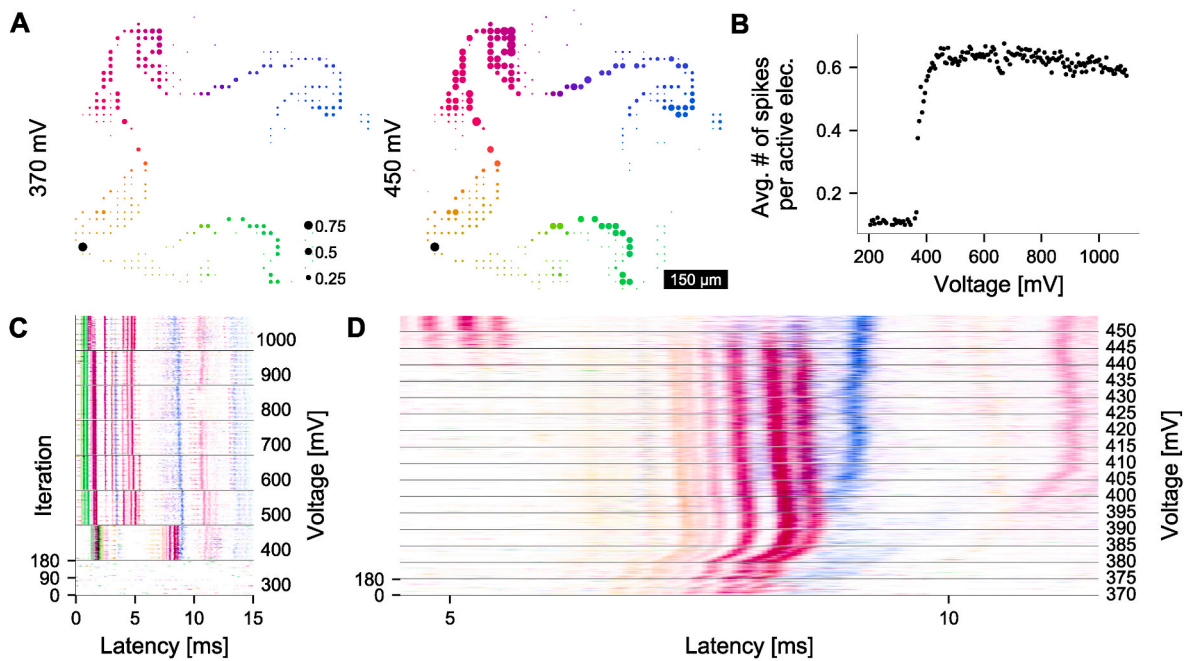
Fig. 4. Stimulating networks with increasing voltage amplitude reveals thresholds, at which spike response patterns change. (A) Activity distribution within the network for stimulation amplitudes of 370 and 450 mV. The dot size corresponds to the number of spikes within the post-stimulus early response on an electrode averaged over 180 trials at 4 Hz. The stimulation electrode is marked in black. **(B)** Average number of spikes in the 15 ms early response across the whole network over the stimulation voltage. Below 350 mV the average lies around the activity threshold of 0.1 spikes per electrode. After a short linear increase around 400 mV the average number of induced spikes reaches a plateau at roughly 0.6 spikes per electrode. **(C)** Post-stimulus raster plot showing the early response for 180 iterations for increasing stimulation amplitudes. While no response is observed at 300 mV, at 500 mV and above an increase of the amplitude causes only minor changes in the response and stable patterns emerge. The color code corresponds to the coloring shown in A. **(D)** Zoom-in to the transition period between 370 mV and 450 mV. While the blue band at 9 ms and the pink band around 11 ms gradually become stronger and shift towards higher latencies, the red bands around 5 ms suddenly appear and remain stable besides a small variation at 1000 mV as seen in **C**. All shown data was recorded from rat cortical neurons at DIV 28.
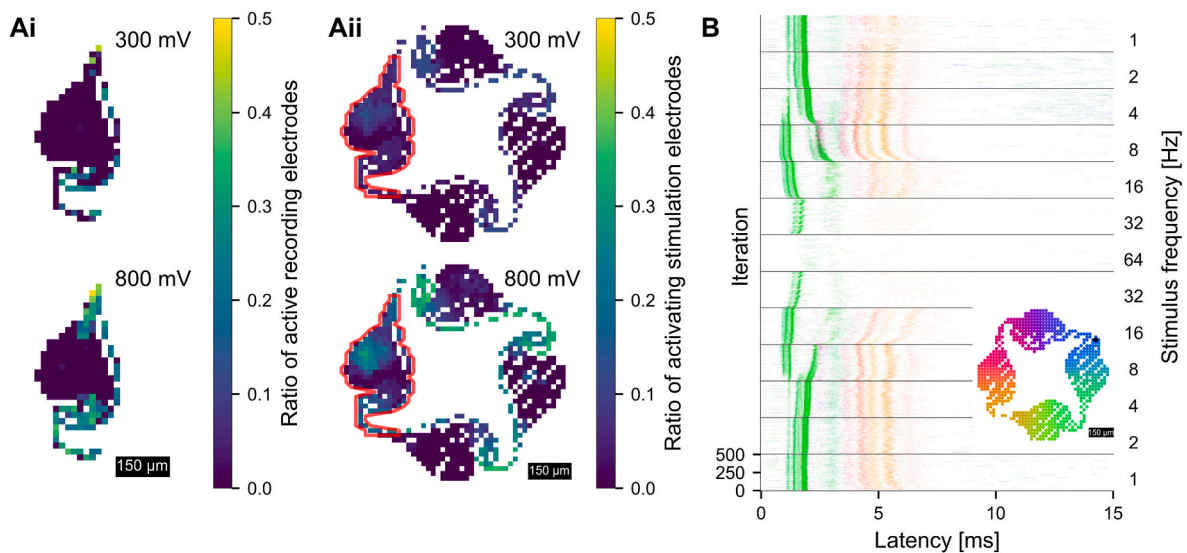

Fig. 5. The post-stimulus early response depends on the stimulation site and frequency. (Ai) Every electrode underlying the left quarter of the network is stimulated for 120 iterations at different amplitudes. The early responses are subsequently thresholded to active recording electrodes. The ratio of active electrodes to all selected recording electrodes of the network is then assigned to each stimulation electrode. In the inter-node and side channel, activity can be induced already at lower stimulation voltages, while triggering a response by stimulating electrodes within the node is unlikely even at higher voltages. This data can be interpreted as a sensitivity map. **(Aii)** Inverse sensitivity map showing for how many of the stimulation electrodes (enclosed in the red boundary) an electrode yields a signal above the active threshold. Activation can be observed inside the stimulated node at higher voltages. The inter-node channels show the highest ratio except for the downstream channel of the stimulated node. **(B)** Modulating the stimulation frequency shows network conditioning and adaptation. Post-stimulus raster plots for 500 stimulus iterations are shown for an exponential frequency sweep from 1 to 64 Hz and back, starting at the bottom of the plot. Between 1 and 4 Hz only minor changes are visible when increasing the frequency. Above 4 Hz an elevated frequency causes increased latency with respect to the stimulus up to ceasing activity at 64 Hz. With decreasing stimulation frequency, the network adapts successively towards the initial pattern. The color-coding of electrodes is according to the map on the bottom right. The stimulation electrode is marked in black. All shown data was recorded using two different cultures of rat cortical neurons at DIV 21.

standard deviation inside the running window for detection-threshold computation to a point that subsequent spikes are not detected anymore. However, it seems that the mentioned problem does not occur for stimulation voltages far above these transitioning points. As the bands jump by more than 2 ms, this could also be caused by earlier recruitment of the underlying axons followed by the refractory period, where they are not responsive. The full plot illustrating the response of the network in 5 mV increments is shown in the supplementary information in Fig. S5. Data from increasing, decreasing, and randomized amplitude modulation on a different network is provided in the supplementary information Fig. S6 and Fig. S7, showing that the transition period is practically unaffected by the stimulation history of a network. The stimulation threshold is also dependent on the electrode material. Data obtained from a network growing on a chip with platinum black coated electrodes (Fig. S6) suggests that a stimulation voltage of 225 mV can already induce a reproducible network answer. Platinum black has a larger porosity compared to platinum. A larger electrode surface offers an increased charge injection capacity (Cogan, 2008), which in turn reduces the stimulation threshold.

3.6. Stimulation efficiency is stimulation-site dependent

Being able to apply an electrical stimulus to any location within engineered neural networks is a substantial advantage offered by CMOS MEAs. Fig. 5A shows the sensitivity of the network to a stimulus applied to electrodes across the whole network in sequence at stimulation voltages of 300 and 800 mV. By varying the stimulation site and determining the number of active electrodes, locations at which the network is most sensitive to stimulation can be visualized. Fig. 5Ai shows this sensitivity for approximately one quarter of an engineered neural network. Consistent with the results shown in previous sections, more electrodes are able to induce a network response at higher stimulation voltages. However, already a stimulation voltage of 300 mV can be sufficient to elicit a network response when the stimulus is applied within the microchannels. Almost every electrode located within a channel is able to induce activity in the network. Channel electrodes not being able to do so may be partially covered and potentially cannot deliver enough charge to depolarize the axons. Within the nodes, an electrical stimulus is generally not able to induce activity. Fig. 5Aii shows results when the question is reversed: How many stimulation electrodes lead to spikes occurring at a specific individual recording electrode? (Here an electrode colored in yellow would indicate that we observe stimulation-induced spikes on this selected electrode for 50 % of the stimulation electrodes in the left network quarter outlined in red.) Again, the electrodes located within the microchannels are easiest to recruit, i.e. are most likely to detect early response activity following stimulation. However, we observe that activity is captured within nodes at higher stimulation voltages, which is especially visible within the node used for stimulation. Figs. S8 and S9 in the supplementary information show the sensitivity maps and inverse sensitivity maps obtained

at all applied stimulation voltages. The post-stimulus raster plots for the data in Fig. 5A at 800 mV are summarized in supplementary movie SM2 (Supplementary Fig. S18 shows one frame of the video, *i.e.* the post-stimulus response for one stimulation electrode), where it is visible that neighboring electrodes can evoke entirely different responses. Supplementary Fig. S10 shows the sensitivity across a whole network on a different culture, revealing similar results for the four compartments.

3.7. Frequency modulation can lead to network conditioning

Another parameter relevant for electrical stimulation is the stimulation frequency. Frequency modulation plays a key role in various mechanisms underlying network plasticity (Wittenberg and Wang, 2006; Bliss and Lømo, 1973; Markram et al., 1997; Feldman, 2012). Fig. 5B shows the post-stimulus raster plots following a stimulus applied to the inter-node channel (black dot in insert showing the color code) with a stimulation voltage of 750 mV at increasing, then decreasing frequencies. The applied frequencies were chosen in logarithmic steps. We observe only minor changes between 1 and 4 Hz. At 8 and 16 Hz, latencies shift towards larger values, as seen in the gradual change of the green band and the red/orange bands, respectively. This change in the early response could be due to the network adapting to the input or a depletion of required ions for signal initiation, *i.e.* some form of short-term plasticity effect. At 16 Hz, a reduction in the spike count is observed with a further reduction at 32 and 64 Hz. This effect might be due to the fact that the cells are not able to follow this high frequency (Gal et al., 2010). However, especially at 64 Hz, the repetitive occurrence of stimulation artifacts may decrease the probability of a spike being detected due to a shift of the standard deviation of the raw signal. Reducing the spike frequency again, more activity is observed, with the green band appearing at 32 Hz at a similar latency as before. Activity at electrodes labeled in orange and yellow occurs again at 16 Hz with bands appearing at 8 Hz. For this frequency, we observe a shift in latency for these bands in opposite direction (earlier latency) compared to the case of increasing frequency. This could be caused by neuron internal effects such as ion availability and conductance (Gal et al., 2010) or network adaptation. Short-term effects due to high-frequency stimulation, known as tetanic stimulation, have also been demonstrated in the literature (Jimbo et al., 1999) and could account for band shifts after the 64 Hz window. Especially when comparing the responses to 8 Hz, strong initial bending of the response bands in opposite directions is visible. We hence observe the potential to influence the response to future stimuli and therefore condition the network with varying stimulation frequencies. This stands in contrast to modulating the stimulation amplitudes, where previously applied stimuli have little to no effect.

3.8. Different activity pathways can be triggered by changing the stimulation site

Varying the stimulation site, we are able to trigger different signaling
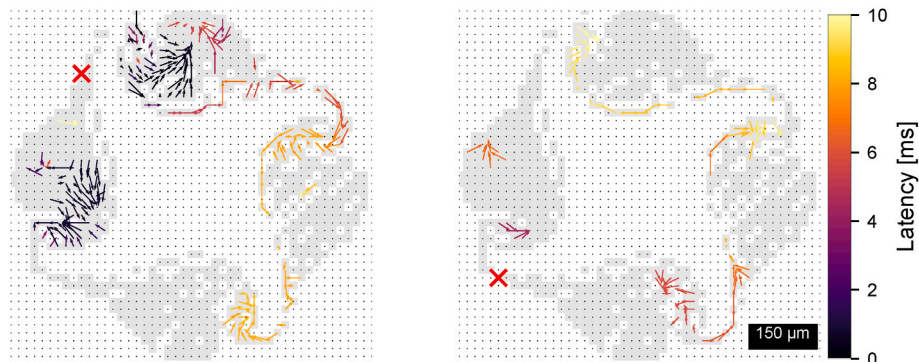

Fig. 6. Different activity propagation pathways can be triggered by varying the stimulation site. Vector fields were used to illustrate the activity flow after stimulation at two electrodes within the same network at DIV 20. Here, the top left inter-node channel and the lower left channel were sequentially stimulated. The stimulation site is marked by a red cross. The induced flow of activity depends on the location of the stimulation despite a constant stimulation amplitude of 800 mV amplitude and stimulation frequency of 4 Hz. Arrows illustrate the direction of information, while the color code indicates the post-stimulus latency at which the information transfer occurred.

pathways through the network within the early response to a stimulus. Similarly as shown before in Fig. 3A, we can illustrate the temporal dynamics of the early response, *i.e.* the propagation of an action potential within the network and along an axon, in a two-dimensional manner. By introducing a vector for every spatially and temporally consecutive spike event as described in the methods section, we can generate vector graphs, that illustrate the flow of information within the network after the stimulus was applied. Fig. 6 shows such vector plots for a stimulus applied to the top-left and the bottom-left inter-node channel. The stimulus applied to the top-left channel resulted in a low-latency propagation of information in the neighboring nodes followed by a clockwise propagation through the microchannels on the right side. The stimulus on the bottom-left channel led to a different flow of information. For example, the activity in the bottom and top right channels is propagating in an anti-clockwise fashion. The activity flow for different stimulus iterations is shown in Supplementary Fig. S13. In both cases locations of 'sinks', *i.e.* points at which vectors terminate and 'sources', *i.e.* points from where vectors originate are visible. Sinks could be attributed to sites at which neurite activity terminates, *i.e.* locations of synapses, while sources may indicate locations of somata. Latency shifts (such as the black-to-orange color change observed in the top node following the stimulation within the top-left channel) could further be interpreted as a synaptic information transfer. Delays occurring between a pre- and a postsynaptic event are within the range of a few milliseconds (O'Lague et al., 1978) and could be visualized and localized with this method.

4. Conclusion and outlook

In this work, we have demonstrated a method to create and interact with engineered biological neural networks on planar CMOS HD-MEAs. We showed that the flat chip topology allows for precise axonal growth confinement using PDMS-based microstructures, which can be adhered to the chip with no intermediate gluing layer. Independent of surface coating and electrode composition, we have obtained spontaneous recordings from engineered networks across their whole spatial extent. Viable networks could be maintained for more than 10 weeks *in vitro*. Besides obtaining spontaneous activity, networks could be flexibly stimulated from any underlying electrode, enabling extensive investigation of the input-output relationship of such small, independent networks. We investigated the spread of the stimulation artifact in different microstructure compartments and assessed the sensitivity of the network to the stimulus. The confinement of axons within microchannels was shown to reduce the voltage stimulation thresholds necessary to induce activity in the network. Post-stimulus responses of engineered neural networks to different stimuli could be recorded with unprecedented detail. We designed an easy-to-use custom data acquisition and analysis toolbox to standardize visualization of the complex activity data. Future work may exploit our datasets to unravel the connectome of the engineered networks.

Stimulation amplitude modulation revealed transition periods, at which different pathways through the network were addressed, yielding changes in the network's post-stimulus response. To further demonstrate the versatility of our system, we modulated the stimulation frequency, which lead to shifts in the post-stimulus latency and revealed a network conditioning effect, *i.e.* a dependency of a response on previous stimuli.

While this work showed network responses to single stimulation sites, the presented methods can be applied to multi-site stimuli, enabling precise stimulation timing at multiple locations in future studies. The connections forming in networks of neurons underlie activity-dependent changes (Feldman, 2012). Hence, the flexibility in defining precisely timed multi-location stimulation patterns on high-density MEAs generates great potential for fundamental plasticity research. By implementing closed-loop stimulation paradigms, as previously demonstrated in the literature (Kagan et al., 2022; Buccelli et al., 2019; An and Nam, 2021) the relevance of *in vitro* engineered neural

networks may be further increased.

Reproducibility is one of the major challenges concerning neuroscience research. We believe that the approach of bottom-up neuroscience, engineering small networks with full control over their connections and full information of the network activity, can be a key to understanding the complexity of the brain. With this work, we showed that PDMS-based microfluidic systems can be combined with novel, flat CMOS HD-MEA technology. This allows future studies to tailor new neural network designs to their specific research questions. Despite the low neural density and topological confinement, our 4-node networks remained highly complex with many interconnecting neurites in each microchannel. The 4-node network design was initially optimized for low-density MEAs. However, planar CMOS MEAs allow for the development of more complex and advanced microstructure designs that effectively utilize the high electrode count and density. The microstructure designs can flexibly be adapted to satisfy a variety of experimental needs. Novel network topologies involving nanochannel designs (Mateus et al., 2022) or the spatial control of synapse formation (Ming et al., 2021) could further increase the predictability of those networks.

Moreover, our approach is compatible with neurons and cells originating from other sources. The used cell source in this work (Sprague-Dawley rats) is widely available (Gileta et al., 2022), however, it is debatable whether findings from such animal models can be applied to understand human biology (Kim et al., 2020). We demonstrated the compatibility and successful microstructure adhesion with secondary laminin coatings, enabling the culturing of hiPSC-derived neurons as has been previously established using low-density glass MEAs (Girardin et al., 2022a). Engineered hiPSC-based networks with stable long-term responses potentially qualify for a preclinical testing platform for individualized medicine, in which disease models could be implemented and exposed to potential drug candidates (Kouroupi et al., 2020).

With the herein presented technology, viable networks can be engineered on CMOS HD-MEAs and studied with unprecedented detail and ease. With this, we hope to facilitate the usage of the platform for systems, computational, and translational neuroscience: The study of neural circuits with low complexity at sub-cellular resolution may enhance our understanding of neural communication and plasticity in the brain. Moreover, such simplified circuits are likely easier to be modeled *in silico* and could eventually provide models to understand the progression of diseases of the nervous system.

CRediT authorship contribution statement

Jens Duru: Conceptualization, Methodology, Software, Investigation, Data Curation, Writing - Original Draft, Visualization, Supervision. **Benedikt Maurer:** Conceptualization, Methodology, Software, Investigation, Data Curation, Writing - Original Draft, Visualization, Supervision. **Ciara Giles Doran:** Software, Validation, Formal Analysis, Data Curation. **Robert Jelitto:** Software, Validation, Formal Analysis. **Joël Küchler:** Software, Validation. **Stephan J. Ihle:** Conceptualization, Methodology, Supervision. **Tobias Ruff:** Conceptualization, Methodology. **Robert John:** Software, Methodology. **Barbara Genocchi:** Data Curation. **János Vörös:** Conceptualization, Project administration, Funding acquisition, Writing - Original Draft.

Declaration of competing interest

The authors have no relevant financial or non-financial interests to disclose.

Data availability

Data will be made available on request.

Acknowledgments

Appendix A. Supplementary data

Supplementary data to this article can be found online at https://doi.org/10.1016/j.bios.2023.115591.

References

Aebersold, M.J., Dermutz, H., Forró, C., Weydert, S., Thompson-Steckel, G., Vörös, J., Demkó, L., 2016. "brains on a chip": towards engineered neural networks. TrAC, Trends Anal. Chem. 78, 60–69.

An, Y., Nam, Y., 2021. Closed-loop control of neural spike rate of cultured neurons using a thermoplasmonics-based photothermal neural stimulation. J. Neural. Eng. 18, 066002.

Bakkum, D.J., Chao, Z.C., Potter, S.M., 2008. Long-term activity-dependent plasticity of action potential propagation delay and amplitude in cortical networks. PLoS One 3, e2088.

von Bartheld, C.S., Bahney, J., Herculano-Houzel, S., 2016. The search for true numbers of neurons and glial cells in the human brain: a review of 150 years of cell counting. J. Comp. Neurol. 524, 3865–3895.

Bliss, T.V.P., Lømo, T., 1973. Long-lasting potentiation of synaptic transmission in the dentate area of the anaesthetized rabbit following stimulation of the perforant path. J. Physiol. 232, 331–356.

Buccelli, S., Bornat, Y., Colombi, I., Ambroise, M., Martines, L., Pasquale, V., Bisio, M., Tessadori, J., Nowak, P., Grassia, F., Averna, A., Tedesco, M., Bonifazi, P., Difato, F., Massobrio, P., Levi, T., Chiappalone, M., 2019. A neuromorphic prosthesis to restore communication in neuronal networks. iScience 19, 402–414.

Chiappalone, M., Bove, M., Vato, A., Tedesco, M., Martinoia, S., 2006. Dissociated cortical networks show spontaneously correlated activity patterns during in vitro development. Brain Res. 1093, 41–53.

Cogan, S.F., 2008. Neural stimulation and recording electrodes. Annu. Rev. Biomed. Eng. 10, 275–309.

Cook, S.J., Jarrell, T.A., Brittin, C.A., Wang, Y., Bloniarz, A.E., Yakovlev, M.A., Nguyen, K.C.Q., Tang, L.T.H., Bayer, E.A., Duerr, J.S., Bülow, H.E., Hobert, O., Hall, D.H., Emmons, S.W., 2019. Whole-animal connectomes of both caenorhabditis elegans sexes. Nature 571, 63–71.

Duru, J., Küchler, J., Ihle, S.J., Forró, C., Bernardi, A., Girardin, S., Hengsteler, J., Wheeler, S., Vörös, J., Ruff, T., 2022. Engineered biological neural networks on high density CMOS microelectrode arrays. Front. Neurosci. 16.

Dworak, B.J., Wheeler, B.C., 2009. Novel MEA platform with PDMS microtunnels enables the detection of action potential propagation from isolated axons in culture. Lab Chip 9, 404–410.

Feldman, D.E., 2012. The spike-timing dependence of plasticity. Neuron 75, 556–571.

FitzGerald, J., Lacour, S., McMahon, S., Fawcett, J., 2008. Microchannels as axonal amplifiers. IEEE (Inst. Electr. Electron. Eng.) Trans. Biomed. Eng. 55, 1136–1146.

Forró, C., Thompson-Steckel, G., Weaver, S., Weydert, S., Ihle, S., Dermutz, H., Aebersold, M.J., Pilz, R., Demkó, L., Vörös, J., 2018. Modular microstructure design to build neuronal networks of defined functional connectivity. Biosens. Bioelectron. 122, 75–87.

Frey, U., Sedivy, J., Heer, F., Pedron, R., Ballini, M., Mueller, J., Bakkum, D., Hafizovic, S., Faraci, F.D., Greve, F., Kirstein, K.U., Hierlemann, A., 2010. Switch-matrix-based high-density microelectrode array in CMOS technology. IEEE J. Solid State Circ. 45, 467–482.

Gal, A., Eytan, D., Wallach, A., Sandler, M., Schiller, J., Marom, S., 2010. Dynamics of excitability over extended timescales in cultured cortical neurons. J. Neurosci. 30, 16332–16342.

Gileta, A.F., Fitzpatrick, C.J., Chitre, A.S., Pierre, C.L.S., Joyce, E.V., Maguire, R.J., McLeod, A.M., Gonzales, N.M., Williams, A.E., Morrow, J.D., Robinson, T.E., Flagel, S.B., Palmer, A.A., 2022. Genetic characterization of outbred sprague dawley rats and utility for genome-wide association studies. PLoS Genet. 18, e1010234.

Girardin, S., Clément, B., Ihle, S.J., Weaver, S., Petr, J.B., Mateus, J.C., Duru, J., Krubner, M., Forró, C., Ruff, T., Fruh, I., Müller, M., Vörös, J., 2022a. Topologically controlled circuits of human iPSC-derived neurons for electrophysiology recordings. Lab Chip 22, 1386–1403.

Girardin, S., Ihle, S.J., Menghini, A., Krubner, M., Tognola, L., Duru, J., Ruff, T., Fruh, I., Müller, M., Vörös, J., 2022b. Engineering Circuits of Human iPSC-Derived Neurons and Rat Primary Glia.

Glover, G.H., 2011. Overview of functional magnetic resonance imaging. Neurosurg. Clin. 22, 133–139.

Gu, C., 2021. Rapid and reversible development of axonal varicosities: a new form of neural plasticity. Front. Mol. Neurosci. 14.

Habibey, R., Latifi, S., Mousavi, H., Pesce, M., Arab-Tehrany, E., Blau, A., 2017. A multielectrode array microchannel platform reveals both transient and slow changes in axonal conduction velocity. Sci. Rep. 7.

Ihle, S.J., Girardin, S., Felder, T., Ruff, T., Hengsteler, J., Duru, J., Weaver, S., Forró, C., Vörös, J., 2022. An experimental paradigm to investigate stimulation dependent activity in topologically constrained neuronal networks. Biosens. Bioelectron. 201, 113896.

Jimbo, Y., Tateno, T., Robinson, H., 1999. Simultaneous induction of pathway-specific potentiation and depression in networks of cortical neurons. Biophys. J. 76, 670–678.

Jonas, E., Kording, K.P., 2017. Could a neuroscientist understand a microprocessor? PLoS Comput. Biol. 13, e1005268.

Jun, J.J., Steinmetz, N.A., Siegle, J.H., Denman, D.J., Bauza, M., Barbarits, B., Lee, A.K., Anastassiou, C.A., Andrei, A., Aydın, Ç., Barbic, M., Blanche, T.J., Bonin, V., Couto, J., Dutta, B., Gratiy, S.L., Gutnisky, D.A., Häusser, M., Karsh, B., Ledochowitsch, P., Lopez, C.M., Mitelut, C., Musa, S., Okun, M., Pachitariu, M., Putzeys, J., Rich, P.D., Rossant, C., lung Sun, W., Svoboda, K., Carandini, M., Harris, K.D., Koch, C., O'Keefe, J., Harris, T.D., 2017. Fully integrated silicon probes for high-density recording of neural activity. Nature 551, 232–236.

Kagan, B.J., Kitchen, A.C., Tran, N.T., Habibollahi, F., Khajehnejad, M., Parker, B.J., Bhat, A., Rollo, B., Razi, A., Friston, K.J., 2022. In vitro neurons learn and exhibit sentience when embodied in a simulated game-world. Neuron 110, 3952–3969 e8.

Kim, J., Koo, B.K., Knoblich, J.A., 2020. Human organoids: model systems for human biology and medicine. Nat. Rev. Mol. Cell Biol. 21, 571–584.

Kongsui, R., Beynon, S.B., Johnson, S.J., Walker, F.R., 2014. Quantitative assessment of microglial morphology and density reveals remarkable consistency in the distribution and morphology of cells within the healthy prefrontal cortex of the rat. J. Neuroinflammation 11.

Kouroupi, G., Antoniou, N., Prodromidou, K., Taoufik, E., Matsas, R., 2020. Patient-derived induced pluripotent stem cell-based models in Parkinson's disease for drug identification. Int. J. Mol. Sci. 21, 7113.

Kriegstein, A., Dichter, M., 1983. Morphological classification of rat cortical neurons in cell culture. J. Neurosci. 3, 1634–1647.

Lancaster, M.A., Renner, M., Martin, C.A., Wenzel, D., Bicknell, L.S., Hurles, M.E., Homfray, T., Penninger, J.M., Jackson, A.P., Knoblich, J.A., 2013. Cerebral organoids model human brain development and microcephaly. Nature 501, 373–379.

Lewandowska, M.K., Bakkum, D.J., Rompani, S.B., Hierlemann, A., 2015. Recording large extracellular spikes in microchannels along many axonal sites from individual neurons. PLoS One 10, e0118514.

Markram, H., Lübke, J., Frotscher, M., Sakmann, B., 1997. Regulation of synaptic efficacy by coincidence of postsynaptic APs and EPSPs. Science 275, 213–215.

Mateus, J.C., Weaver, S., van Swaay, D., Renz, A.F., Hengsteler, J., Aguiar, P., Vörös, J., 2022. Nanoscale patterning of in Vitro neuronal circuits. ACS Nano 16, 5731–5742.

Miller, J.D., Ganat, Y.M., Kishinevsky, S., Bowman, R.L., Liu, B., Tu, E.Y., Mandal, P.K., Vera, E., won Shim, J., Kriks, S., Taldone, T., Fusaki, N., Tomishima, M.J., Krainc, D., Milner, T.A., Rossi, D.J., Studer, L., 2013. Human iPSC-based modeling of late-onset disease via progerin-induced aging. Cell Stem Cell 13, 691–705.

Ming, Y., Abedin, M.J., Tatic-Lucic, S., Berdichevsky, Y., 2021. Microdevice for directional axodendritic connectivity between micro 3d neuronal cultures. Microsystems & Nanoengineering 7.

Mossink, B., Verboven, A.H., van Hugte, E.J., Gunnewiek, T.M.K., Parodi, G., Linda, K., Schoenmaker, C., Kleefstra, T., Kozicz, T., van Bokhoven, H., Schubert, D., Kasri, N. N., Frega, M., 2021. Human neuronal networks on micro-electrode arrays are a highly robust tool to study disease-specific genotype-phenotype correlations in vitro. Stem Cell Rep. 16, 2182–2196.

Müller, J., Ballini, M., Livi, P., Chen, Y., Radivojevic, M., Shadmani, A., Viswam, V., Jones, I.L., Fiscella, M., Diggelmann, R., Stettler, A., Frey, U., Bakkum, D.J., Hierlemann, A., 2015. High-resolution CMOS MEA platform to study neurons at subcellular, cellular, and network levels. Lab Chip 15, 2767–2780.

Nogueira, G.O., Garcez, P.P., Bardy, C., Cunningham, M.O., Sebollela, A., 2022. Modeling the human brain with ex vivo slices and in vitro organoids for translational neuroscience. Front. Neurosci. 16.

Obien, M.E.J., Deligkaris, K., Bullmann, T., Bakkum, D.J., Frey, U., 2015. Revealing neuronal function through microelectrode array recordings. Front. Neurosci. 8.

O'Lague, P.H., Potter, D., Furshpan, E., 1978. Studies on rat sympathetic neurons developing in cell culture. Dev. Biol. 67, 384–403.

Pan, L., Alagapan, S., Franca, E., DeMarse, T., Brewer, G.J., Wheeler, B.C., 2014. Large extracellular spikes recordable from axons in microtunnels. IEEE Trans. Neural Syst. Rehabil. Eng. 22, 453–459.

Penney, J., Ralvenius, W.T., Tsai, L.H., 2019. Modeling alzheimer's disease with iPSC-derived brain cells. Mol. Psychiatr. 25, 148–167.

Reinartz, S., Biro, I., Gal, A., Giugliano, M., Marom, S., 2014. Synaptic dynamics contribute to long-term single neuron response fluctuations. Front. Neural Circ. 8.

Renault, R., Durand, J.B., Viovy, J.L., Villard, C., 2016. Asymmetric axonal edge guidance: a new paradigm for building oriented neuronal networks. Lab Chip 16, 2188–2191.

Ronchi, S., Fiscella, M., Marchetti, C., Viswam, V., Müller, J., Frey, U., Hierlemann, A., 2019. Single-cell electrical stimulation using CMOS-based high-density microelectrode arrays. Front. Neurosci. 13.

Schröter, M., Wang, C., Terrigno, M., Hornauer, P., Huang, Z., Jagasia, R., Hierlemann, A., 2022. Functional imaging of brain organoids using high-density microelectrode arrays. MRS Bull. 47, 530–544.

Shadmani, A., Viswam, V., Chen, Y., Bounik, R., Dragas, J., Radivojevic, M., Geissler, S., Sitnikov, S., Muller, J., Hierlemann, A., 2019. Stimulation and artifact-suppression

techniques for *in Vitro* high-density microelectrode array systems. IEEE (Inst. Electr. Electron. Eng.) Trans. Biomed. Eng. 66, 2481–2490.

Sharf, T., van der Molen, T., Glasauer, S.M.K., Guzman, E., Buccino, A.P., Luna, G., Cheng, Z., Audouard, M., Ranasinghe, K.G., Kudo, K., Nagarajan, S.S., Tovar, K.R., Petzold, L.R., Hierlemann, A., Hansma, P.K., Kosik, K.S., 2022. Functional neuronal circuitry and oscillatory dynamics in human brain organoids. Nat. Commun. 13.

Shepherd, G.M.G., Raastad, M., Andersen, P., 2002. General and variable features of varicosity spacing along unmyelinated axons in the hippocampus and cerebellum. Proc. Natl. Acad. Sci. USA 99, 6340–6345.

Shimba, K., Chang, C.H., Asahina, T., Moriya, F., Kotani, K., Jimbo, Y., Gladkov, A., Antipova, O., Pigareva, Y., Kolpakov, V., Mukhina, I., Kazantsev, V., Pimashkin, A., 2019. Functional scaffolding for brain implants: engineered neuronal network by microfabrication and iPSC technology. Front. Neurosci. 13.

Viswam, V., Obien, M.E.J., Franke, F., Frey, U., Hierlemann, A., 2019. Optimal electrode size for multi-scale extracellular-potential recording from neuronal assemblies. Front. Neurosci. 13.

Wittenberg, G.M., Wang, S.S.H., 2006. Malleability of spike-timing-dependent plasticity at the CA3-CA1 synapse. J. Neurosci. 26, 6610–6617.

Yuan, X., Schröter, M., Obien, M.E.J., Fiscella, M., Gong, W., Kikuchi, T., Odawara, A., Noji, S., Suzuki, I., Takahashi, J., Hierlemann, A., Frey, U., 2020. Versatile live-cell activity analysis platform for characterization of neuronal dynamics at single-cell and network level. Nat. Commun. 11.

Zhou, A., Johnson, B.C., Muller, R., 2018. Toward true closed-loop neuromodulation: artifact-free recording during stimulation. Curr. Opin. Neurobiol. 50, 119–127.